Contents lists available at SciOpen

Food Science and Human Wellness

journal homepage: https://www.sciopen.com/journal/2097-0765

China Food Publishing Co.

A pH-responsive ZIF-8-encapsulation Au nanocluster fluorescent probe applying for convenient and efficient detection of glucose

Mingfei Pan, Yixin Wang, Hao Wang, Xuan Liu, Xiaochun Hu, Dan Zhang, Shuo Wang*

State Key Laboratory of Food Nutrition and Safety, Key Laboratory of Food Quality and Health of Tianjin, Tianjin University of Science and Technology, Tianjin 300457, China

ARTICLE INFO

Article history:
Received 6 April 2024
Received in revised form 5 May 2024
Accepted 19 August 2024

Keywords:
Glucose
Au nanoclusters
Aggregation-induced emission
Zeolite imidazole framework (ZIF-8)
pH-responsive

ABSTRACT

Glucose plays a crucial role in maintaining human health as an indispensable source of energy in living organisms. Accurate monitoring of glucose levels in living organisms and detecting it in food is essential. In this study, gold nanoclusters (AuNCs) with unique aggregation-induced emission (AIE) effects were encapsulated within zeolite imidazole framework (ZIF-8) to fabricate a pH-responsive AuNCs@ZIF-8 fluorescent nanocomposite. The fluorescence intensity had significant sevenfold enhancement compared to AuNCs alone due to the structural domain-limiting effects exerted by ZIF-8, which effectively inhibited the rotations and vibrations of the AuNCs ligands. Based on the increased acidity generated by glucose catalytic oxidation *via* glucose oxidase (GOx), the subsequent degradation of ZIF-8 structure and the consequent reduction of AuNCs with AIE effects were achieved, and a rapid and efficient fluorescence quantification for glucose was performed. The constructed AuNCs@ZIF-8-based fluorescent probe demonstrated a favorable linear response to glucose, achieving a detection limit of 0.096 mmol/L and providing a rapid and efficient approach suitable for assessing glucose levels in both blood and beverage samples.

1. Introduction

Glucose oxidation, a fundamental metabolic process in living organisms, holds immense importance in supplying energy to biological cells and supporting various physiological functions[1-2]. Blood glucose levels serve as a critical indicator of human health status, typically falling within the range of 3.9−6.0 mmol/L when measured in a fasting state[3]. Deviations from these normal levels can lead to a variety of health problems, such as hypoglycemia, cardiovascular disease, diabetes, and associated complications, posing significant risks to individual health[4-5]. In addition, glucose is a vital additive ingredient in food fields and commonly incorporated to enhance the taste and quality of food products, especially in glucose-containing beverages[6]. Over consumption of glucose can adversely affect organs such as the liver and kidneys and disrupt normal physiological functions[7]. Therefore, it is imperative to develop rapid, convenient, and efficient strategies for the surveillance and quantitation of glucose levels in blood and food to maintain human health and food safety.

Up to this point, a variety of analytical methods based on different principles have been explored and applied for detecting glucose targets in clinical samples or food testing processes. These methods encompassed techniques such as high-performance liquid chromatography (HPLC) for chromatographic separation[8], surface-enhanced Raman scattering (SERS) employing noble metals[9],

* Corresponding author at: State Key Laboratory of Food Nutrition and Safety, Tianjin University of Science and Technology, Tianjin 300457, China.
Email address: s.wang@tust.edu.cn (S. Wang)
Peer review under responsibility of Beijing Academy of Food Sciences.

SciOpen Publishing services by Tsinghua University Press

http://doi.org/10.26599/FSHW.2024.9250392

electrochemical analysis[10-11], fluorescence and colorimetric[12]. Among the array of techniques utilized for detecting glucose targets in clinical samples or food testing, fluorescence sensing analysis strategies have attracted significant attention owing to their sensitivity, operational simplicity, and cost-effectiveness. Considering that glucose does not have naturally fluorescence due to its small molecular size, enzymatic catalysis is commonly required to generate specific substances for detection. Glucose oxidase (GOx) has become the enzyme of choice for glucose detection, favored for its robust activity, remarkable specificity, and cost-effectiveness. Most of the prevailing glucose sensing strategies involved immobilizing GOx on the sensing interface and quantifying the amount of H_2O_2 produced through its catalytic action of glucose substrates to facilitate glucose detection[13-14]. Sun et al.[15] reported an ultrasensitive fluorescent biosensor to be used for glucose detection based on a Fenton-like reaction triggered chemical redox-cycling signal amplification strategy, with a limit of detection (LOD) of 0.3 nmol/L. Therefore, it can provide a strategy for developing low-cost and sensitive methods for biological and clinical diagnostics applications[16]. However, the immobilization of GOx at the sensing interface is prone to deactivation during prolonged storage, potentially compromising assay sensitivity and resulting inaccurate results. Therefore, there is significant research value in creating a novel and efficient fluorescence sensing strategy for glucose that aimed at improving the convenience, sensitivity, and stability of glucose detection methods.

As a class of ideal fluorescent nanomaterials, metal nanoclusters (MNCs) such as Au, Ag, Cu, have attracted increasing interest. The luminescence performance of MNCs can generally be improved through strategies such as fluorescence resonance energy transfer (FRET), antenna effect (AE) and aggregation-induced emission (AIE), etc., among which the AIE effect is gradually becoming a research hotspot. Wang et al.[17] found the fluorescence intensity of copper nanoclusters (CuNCs) is enhanced strongly through the glutathione (GSH)-controlled AIE enhancement of self-assembled CuNCs. Wang et al.[18] reported a kind of specific structure of self-assembled CuNCs, greatly enhancing the fluorescence emission intensity of tetracycline (TC). Inspired by these reports, the application of the AIE-type gold nanoclusters (AuNCs) composite materials were investigated. The AuNCs, among various MNCs, have great application prospects in various fields such as bioimaging, optical sensing and nanocatalysis by virtue of their more excellent stability[19-21]. Despite the AuNCs effectively overcoming aggregation-caused quenching (ACQ), a common issue with conventional organic luminescent materials, their lower fluorescence quantum yield (QY) has largely restricted their broad application. The AIE effects are a typical photophysical phenomenon, and weakly fluorescent or no-fluorescent materials exhibit specific fluorescence enhancement when in an aggregated state due to the restriction of molecules (or ligands) motion[22]. This unique and controllable effects have been applied to enhance the fluorescence intensity of certain nanomaterials, thus expanding their range of applications in fluorescence-based technologies. Synthesizing with thiolate ligands and utilizing GSH as a reductant and stabilizer, AuNCs demonstrated a typical core-shell structure and AIE properties. When aggregated, the intramolecular vibrations and rotations of the surface ligands are restricted, thus suppressing the non-radiative transition of the excited state associated with the ligands, resulting in pronounced fluorescence enhancement[23]. Moreover, synthesizing AIE-type AuNCs is straightforward and controllable, making it an effective strategy for producing AuNCs material with tunable fluorescence intensity[24].

Metal-organic frameworks (MOFs) are a class of materials assembled from specific metal ions and organic ligands, showcasing characteristics such as orderly pore structures, high loading capacities, and exceptional stability[25]. Zeolite imidazole framework (ZIF-8), a type of MOFs, has attracted considerable attention due to its simple preparation process, high porosity, and sensitive response to pH values[26]. It is promising for various applications in adsorption, curing, and encapsulation of small-molecule targets, biological proteins, and others. Benefiting from the high porosity of MOFs, AIE luminogens (AIEgens) or nanomaterials with AIE characteristics can be encapsulated as guests into MOFs. Leveraging the excellent luminescent properties of AIE materials and the unique hollow structure of MOFs, hydrogen bonds or coordination bonds can be formed with guest molecules to influence fluorescence emission, facilitating the quantitative detection of target analytes. For instance, Xie et al.[27] successfully synthesized luminescent metal-organic frameworks (LMOFs) by incorporating AIEgens into ZIF-8, enhancing the fluorescence emission efficiency while retaining the AIE characteristics. They developed a fluorescent colorimetric paper strip utilizing LMOF-2 with GOx for visual detection of glucose in serums. This method demonstrated outstanding performance within the normal fasting blood glucose range of 3−8 mmol/L, offering a novel solution for glucose monitoring. Hence, by exploiting the domain-limiting effects of the ZIF-8 framework, the induced aggregation of AuNCs significantly enhanced the fluorescence efficiency and effectively improved self-capability to resist external environmental interference, thereby improving fluorescence stability and laying the groundwork for the development of fluorescence analysis strategies[28-29].

In this study, a fluorescent strategy for detecting glucose targets was introduced by encapsulating AIE-type AuNCs within the ZIF-8 structure (Fig. 1). ZIF-8 underwent self-assembled around the aggregated AuNCs, resulting in a significant enhancement in their fluorescence emission efficiency. Upon GOx catalysis of glucose targets and subsequent alterations in environmental acidity, protonation of the methylimidazole ligands linkers in ZIF-8 occurred, disrupting the coordination with Zn^{2+} ions and leading to the decomposition of the framework[30]. The ZIF-8 framework decomposed and removed the aggregation effects of AuNCs, thus enabling rapid and efficient detection of glucose targets.

2. Material and methods

2.1 Reagents and materials

Glucose (99.7%), sucrose (99.7%), and *L*-ascorbic acid (99.7%) were purchased from Tianjin Chemical Reagent No.1 Factory (Tianjin, China). GSH (98.0%), *D*-xylose (99.0%), *D*-galactose and *D*-maltose monohydrate (98.0%) were procured from Soleibao Technology Co., Ltd. (Beijing, China). GOx (180 U/mg) and 1*H*-purine-2,6,8(3*H*,7*H*,9*H*)-trione (98.0%) from *Aspergillus niger* were obtained from Aladdin Chemical Reagent Co., Ltd. (Shanghai, China). *L*-Cysteine (99.0%), *D*-serine (98.5%), gold (III) chloride trihydrate ($HAuCl_4 \cdot 3H_2O$, 99.9%) and 2-methylimidazole (2-MI, 99.0%)

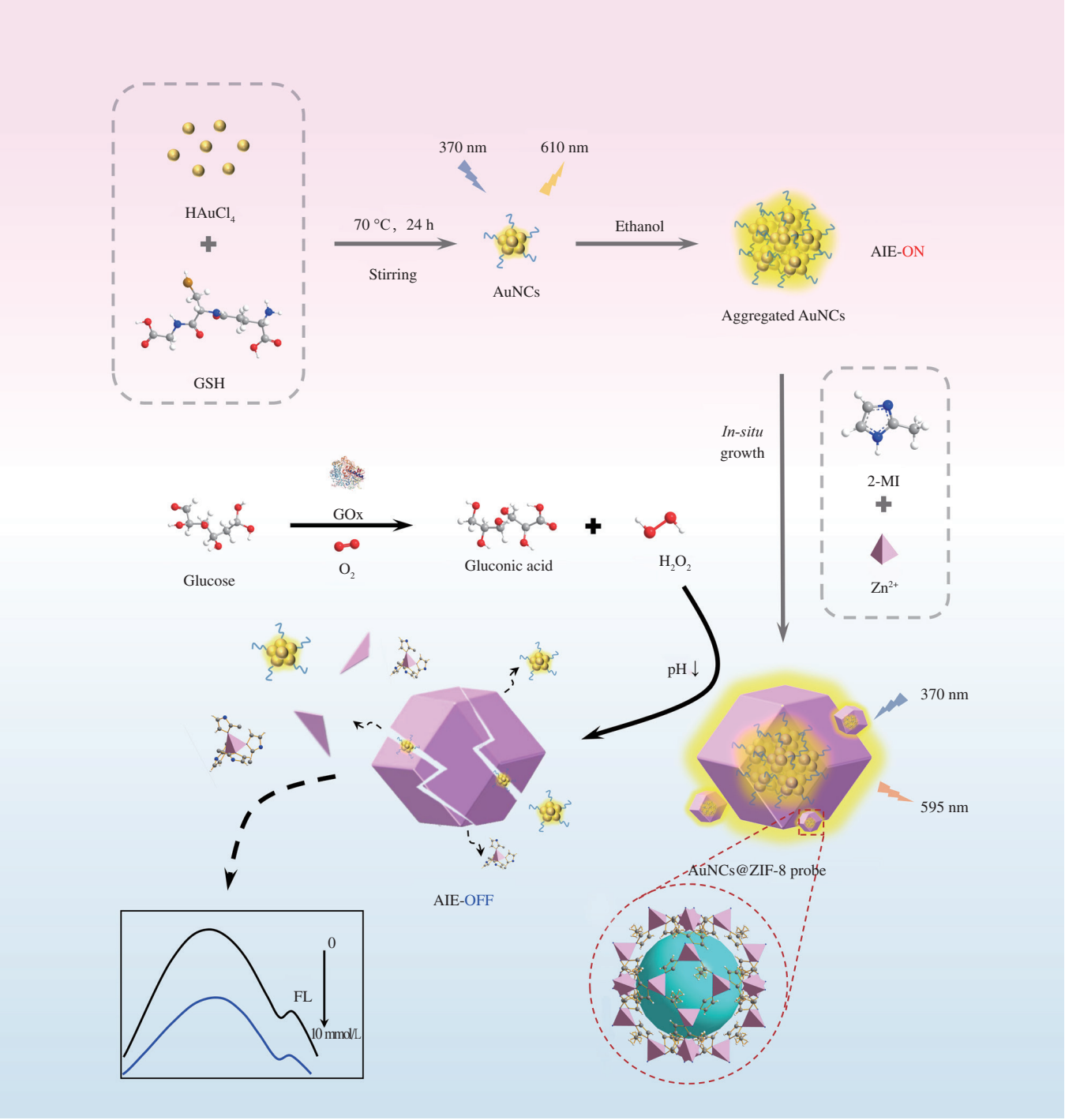

Fig. 1 Schematic diagram of preparation of AuNCs@ZIF-8 fluorescent probe for glucose fluorescence detection.

was received from Macklin Biochemical Co., Ltd. (Shanghai, China). The reagents methanol, ethanol, zinc nitrate hexahydrate ($Zn(NO_3)_2 \cdot 6H_2O$, 99.0%), and hydrogen peroxide (H_2O_2, 30.0%) were purchased from Sinopharm Chemical Reagent Co., Ltd. (Shanghai, China). Ultrapure water was produced using a Milli-Q Purification System (18 MΩ·cm, Millipore, USA).

2.2 Instrumentation

The structures and morphologies of AuNCs, ZIF-8, and AuNCs@ZIF-8 were characterized by transmission electron microscopy (TEM, Talos G2 200X, Thermo, USA) and scanning electron microscopy (SEM, Apreo, Thermo, USA). The crystal surfaces of the materials were characterized using an X-ray diffractometer (XRD, D8 Advance, Bruker, Germany) within a 2θ range of 5°–90° and a scanning speed

of 5°/min. The composition and valence states of AuNCs@ZIF-8 were studied using X-ray photoelectron spectroscopy (XPS) obtained by Scientific EscaLab 250Xi (Thermo, USA). Fourier transform infrared spectroscopy (FT-IR) spectra were obtained using a Nicolet iS50 spectrometer (Thermo, USA). The specific surface area was determined by N_2 adsorption at 77 K using a BELSORP-max II instrument (Microtrac BEL, Japan). Thermogravimetric analyzer (TGA, Q50, TA, USA) was employed to verify the stability and composition of the fluorescent probe. Ultraviolet-visible (UV-vis) spectra and fluorescence spectra were recorded using an ultraviolet spectrophotometer (UV-2600, Shimadzu, Japan) and a fluorescence spectrophotometer (Lumina, Thermo, USA).

2.3 Synthesis of the AIE-type AuNCs

The AIE-type AuNCs utilized in this work were synthesized through the reduction of $HAuCl_4$ using GSH. Specifically, 1.0 mL of $HAuCl_4$ (18 mmol/L) and 0.3 mL of GSH (100 mmol/L) were mixed in ultrapure water. As the solution's color shifted from a light yellow to transparent, the volume was adjusted to 10.0 mL with ultrapure water. Subsequently, the solution was heated to 70 °C, away from light, and gently stirred for 24 h. The resulting light-yellow solution containing the AIE-type AuNCs was then stored in the dark at 4 °C for subsequent use.

2.4 Preparation of AuNCs@ZIF-8 nanocomposite

The preparation of the AuNCs@ZIF-8 nanocomposite involved the *in-situ* synthesis of ZIF-8 around the AIE-type AuNCs. Initially, 4.0 mL of the prepared AuNCs solution was mixed with an equal volume of ethanol, and centrifuged at 10 000 r/min for 15 min. The resulting precipitated AuNCs were re-dispersed in 2.0 mL of methanol, followed by the addition of 10.0 mL of $Zn(NO_3)_2{\cdot}6H_2O$ (30 mmol/L) and 10.0 mL of 2-MI (90 mmol/L). The mixture was subjected to magnetic stirring for 5 min and subsequently sonicated for 40 min avoiding light. Finally, the solid product was collected by centrifugation, thoroughly washed with methanol, freeze-dried, and stored in the dark at 4 °C for subsequent use.

2.5 Fluorescent probe based AuNCs@ZIF-8 for glucose detection

The fluorescence detection process of the glucose targets using the prepared AuNCs@ZIF-8 probe involved the following steps: 75 μL of glucose working solutions at concentrations ranging from 1 to 10 mmol/L were accurately prepared and thoroughly mixed with 25 μL of GOx (2.7 U) and 100 μL of PBS (10 mmol/L, pH 6.5). A total of 50 μL of the prepared AuNCs@ZIF-8 solution (5 mg/mL) was added to the aforementioned reaction system, which was then diluted to a total volume of 500 μL using ultrapure water. The entire system was then subjected to incubation in a 37 °C water bath for 30 min. Subsequently, the fluorescence spectrum of the resulting solution system were analyzed and the fluorescence maxima at wavelength from 500 to 700 nm were recorded for the calculation of glucose contents. The LOD was determined based on the slope (k) of the calibration curve obtained from the fluorescence response of the AuNCs@ZIF-8 probe to various concentrations of glucose. It was calculated using the formula 3 σ/k, where σ represents the standard deviation of the blank and k represents the slope of the calibration curve.

2.6 Analysis of glucose in real samples

To assess the practical utility of the prepared AuNCs@ZIF-8 probe in glucose measurement, fresh blood samples obtained from healthy volunteers and commercially available glucose beverages were employed as real samples for fluorescence detection. The sample measurement process was described as follows: 75 μL of either blood or beverage samples were accurately measured and subsequently centrifuged at 12 000 r/min for 10 min. The resulting supernatant from beverage samples underwent a 50-fold dilution with ultrapure water, while no further treatment was necessary for the supernatant of the blood samples. Then, 75 μL of the treated sample was mixed with 25 μL of GOx (2.7 U) and 100 μL PBS, followed by the addition of 50 μL of the prepared AuNCs@ZIF-8 solution (5 mg/mL) and 250 μL of ultrapure water for fluorescence analysis after incubation at 37 ℃ for 30 min. Three levels of glucose (1, 4, and 7 mmol/L) were added to each of the 3 beverage samples, and a prepared fluorescent probe was applied for glucose detection.

3. Results and discussions

3.1 Preparation of AuNCs@ZIF-8 probe and glucose detection principle

Fig. 1 presented the schematic diagram of the preparation and operational mechanism of the AuNCs@ZIF-8 probe. Initially, the AIE-type AuNCs were synthesized through the "one-pot method", with GSH serving as both stabilizer and reductant. Subsequently, the dispersed AuNCs were induced to aggregate in the presence of the organic solvent ethanol, activating the AIE effects. The Zn^{2+} ions interacted with $-COO^-$ groups on the ligands of AuNCs, which formed the ZIF-8 framework through interaction with the N atoms of 2-MI, facilitating the successful self-assembly of ZIF-8 around AuNCs. The confined space within the ZIF-8 structure restricted the distance between the AuNCs, enhancing the interactions of their surface groups, and limited the vibrations and rotations of the surface ligands, promoting further aggregation of AuNCs. This enhanced aggregation activated the energy transition from non-radiative to radiative, resulting in strong fluorescence emission from the AuNCs@ZIF-8 nanocomposite. Under acidic conditions, the protonation of methylimidazole ligands linkers occurred, disrupting the coordination between Zn^{2+} ions and the imidazole rings, making the ZIF-8 structure sensitive to acidity. In the presence of oxygen, glucose molecule was catalytically decomposed by GOx into gluconic acid and H_2O_2 (Eq. 1), consequently increasing the acidity in the microenvironment.

$$\text{Glucose} + O_2 + H_2O \xrightarrow{\text{GOx}} \text{Gluconic acid} + H_2O_2 \quad (1)$$

This heightened acidity can cause the breakdown of the ZIF-8 structure, leading to the release of internally confined AuNCs and a subsequent reduction in the fluorescence intensity of the system. Based on this decrease in fluorescence intensity, the quantitative analysis of glucose targets can be achieved.

3.2 Characterization of AIE-type AuNCs and AuNCs@ZIF-8 nanocomposite

TEM analysis showed that the resulting AIE-type AuNCs displayed a uniform spherical morphology, with an average diameter of approximately 1.57 nm (Figs. 2A and B). This ultra-small size promoted the formation of aggregated states, which endowed them with distinctive luminescent properties and a high QY. Additionally, the aggregation of presynthesized AuNCs were induced by ethanol, an undesired solvent. Subsequently, the self-assembly of ZIF-8 around the aggregated AuNCs was achieved through ultrasound-assisted precipitation, forming the AuNCs@ZIF-8 nanocomposite. As shown in Fig. S1, the colors of AuNCs in solution (visible: light-yellow; UV: orange) and initial ZIF-8 solid powder (visible: white; UV: blue) contrasted starkly with the AuNCs@ZIF-8 powder acquired subsequent to the embedding of AuNCs, which exhibited a light-yellow color under visible light and a distinct bright yellow color under UV irradiation. The morphological characteristics of ZIF-8 before and after being embedded in AuNCs were investigated using TEM and SEM. As illustrated in Figs. 2C, D and F, the crystal morphology of the synthesized AuNCs@ZIF-8 nanocomposite closely resembled that of pristine ZIF-8, with an average particle size maintained at approximately 132.6 nm. Notably, this smaller particle sizes of ZIF-8 provided a higher specific surface area and greater interaction with the external environment. Conversely, the larger particle sizes contributed to the formation of oversized pores, permitting the escape of AuNCs from ZIF-8 structure. Additionally, it retained a complete rhombic dodecahedral structure (Fig. 2E), with noticeable aggregations of AuNCs clearly visible within. To further investigate the distribution of AuNCs within the ZIF-8 framework, high-angle annular dark-field scanning TEM (HAADF-STEM) was employed to analyze the presence of corresponding elements (Fig. 2G). The results exhibited a uniform dispersion of Zn, N, Au, and S elements within the AuNCs@ZIF-8 nanostructure. This observation not only validated the existence of AuNCs within the ZIF-8 framework but also underscored that the introduction of AuNCs did not change the original morphology of ZIF-8.

XRD was employed to investigate the crystal structure and composition of AuNCs@ZIF-8 nanocomposite. In Fig. 3A, characteristic peaks for the (011), (002), (112), (022), (013), (222), (114), (233), (134), (044), and (244) crystal planes of typical ZIF-8 were noted at corresponding 2θ values of 7.38°, 10.45°, 12.82°, 14.83°, 16.61°, 18.17°, 22.27°, 24.59°, 26.84°, 29.77°, and 30.69°, respectively. Additionally, distinct diffraction peaks of AuNCs@ZIF-8 appeared at 2θ values of 7.43°, 10.51°, 12.85°, 14.85°, 16.58°, 18.17°, 22.23°, 24.62°, 26.80°, 29.77°, and 30.72°, demonstrating structural similarity with ZIF-8 and indicating that the encapsulation of AuNCs did not affect the crystal structure growth of ZIF-8. The slight shifts observed in the characteristic peaks implied minor alterations in lattice distances after modification. Fig. 3B displayed the FT-IR results of AuNCs@ZIF-8 and ZIF-8. Both materials exhibited broad absorption bands within the range of 3 000−3 300 cm^{-1} primarily attributed to −OH bonds. In pure ZIF-8, the bands at 2 927 and 3 130 cm^{-1} were assigned to C−H stretching in the aromatic and aliphatic groups of imidazole, respectively, while bands at 1 308 and 1 581 cm^{-1} corresponded to the stretching vibrations of the C−N and C=N groups. Characteristic peaks of stretching vibrations of the imidazole rings were found in the spectral region 600−1 500 cm^{-1}, alongside a distinctive band at 421 cm^{-1} attributed to Zn–N stretching, characteristic of the ZIF-8 structure. Notably, the presence of a distinct Zn−O peak at 525 cm^{-1} in the AuNCs@ZIF-8 spectrum indicated that the formation of AuNCs@ZIF-8 relied on the coordination between Zn^{2+} ions and $-COO^-$ in GSH. Furthermore, the elemental charge states were investigated through XPS experiments. As illustrated in Fig. 3C, the measured spectrum of the AuNCs@ZIF-8 nanocomposite exhibited 6 prominent peaks around Au 4f, S 2p, C 1s, N 1s, O 1s, and Zn 2p, confirming the presence of significant elements, including Zn, O, C, N, S, and Au in AuNCs@ZIF-8. High-resolution XPS spectra for Au and Zn (Figs. 3D and E) revealed specific features. The Au 4f spectrum of AuNCs@ZIF-8 showed 2 peaks at 88.0 and 84.0 eV, corresponding to Au $4f_{5/2}$ and Au $4f_{7/2}$ of AuNCs, and The Zn 2p and Zn 3p spectrum had 2 peaks at 1 044.65, 1 021.55 and 97.15, 89.05 eV, respectively, corresponding to Zn $2p_{1/2}$, Zn $2p_{3/2}$ and Zn $3p_{1/2}$, Zn $3p_{3/2}$ of AuNCs.

The N_2 isothermal adsorption-desorption curves of AuNCs@ZIF-8 and ZIF-8 (Figs. S2A and B) both exhibited typical type I isotherms, indicative of their characteristic microporous structures and robust adsorption capacities. The encapsulation of AuNCs led to a specific surface area of 1 779.18 m^2/g and a pore volume of 0.425 m^2/g for the prepared AuNCs@ZIF-8 nanocomposite, slightly lower than those of pure ZIF-8 (1 947.03, 0.714 m^2/g). Using density functional theory (DFT), the average micropore sizes of AuNCs@ZIF-8 and ZIF-8 were determined to be 2.38 and 2.91 nm, respectively (Figs. S2C and D). These results indicated that the AuNCs@ZIF-8 nanocomposite maintained the microporous structure of ZIF-8, confirming that the AuNCs were encapsulated in ZIF-8 structure rather than being embedded in its pores. The TGA curves displayed in Fig. 3F demonstrated that the structure of ZIF-8 breakdown occurred at 600 °C, correlating with a significant weight loss rate of 71.92%. Notably, this thermal decomposition temperature closely aligned with that of AuNCs@ZIF-8, which exhibited a weight loss rate of approximately 84.11%. This similarity in thermal decomposition temperatures suggested that the AuNCs@ZIF-8 nanocomposite inherited the high thermal stability characteristic of ZIF-8.

3.3 Optical properties and stability study of AuNCs and AuNCs@ZIF-8

The study conducted a comprehensive analysis of the optical properties of the prepared AuNCs and AuNCs@ZIF-8 materials. As illustrated in Fig. 4A, the UV spectra of the synthesized AIE-type AuNCs displayed a unique absorption peak at approximately 400 nm, a typical feature distinguishing them from other AuNCs. Comparison of the UV absorption spectrum of ZIF-8 within the 300−500 nm range showed a remarkable similarity with the spectra of the AuNCs@ZIF-8 nanocomposite. With an increase in the excitation wavelength (E_X) (350−400 nm), the emission wavelength (E_M) of AuNCs@ZIF-8 remained constant (Fig. 4B). At an E_X of 370 nm, the fluorescence intensity of AuNCs@ZIF-8 peaked at 595 nm. Consequently, the optimal E_X and E_M of AuNCs@ZIF-8 were established at 370 and 595 nm, respectively. Fig. 4C exhibited that pure ZIF-8 lacks an emission peak, contrasting sharply with the AuNCs@ZIF-8 nanocomposite, which displayed a distinct emission peak at 595 nm with a fluorescence intensity approximately 7 times greater than that of the AuNCs at 610 nm. This observation suggested that the fluorescence

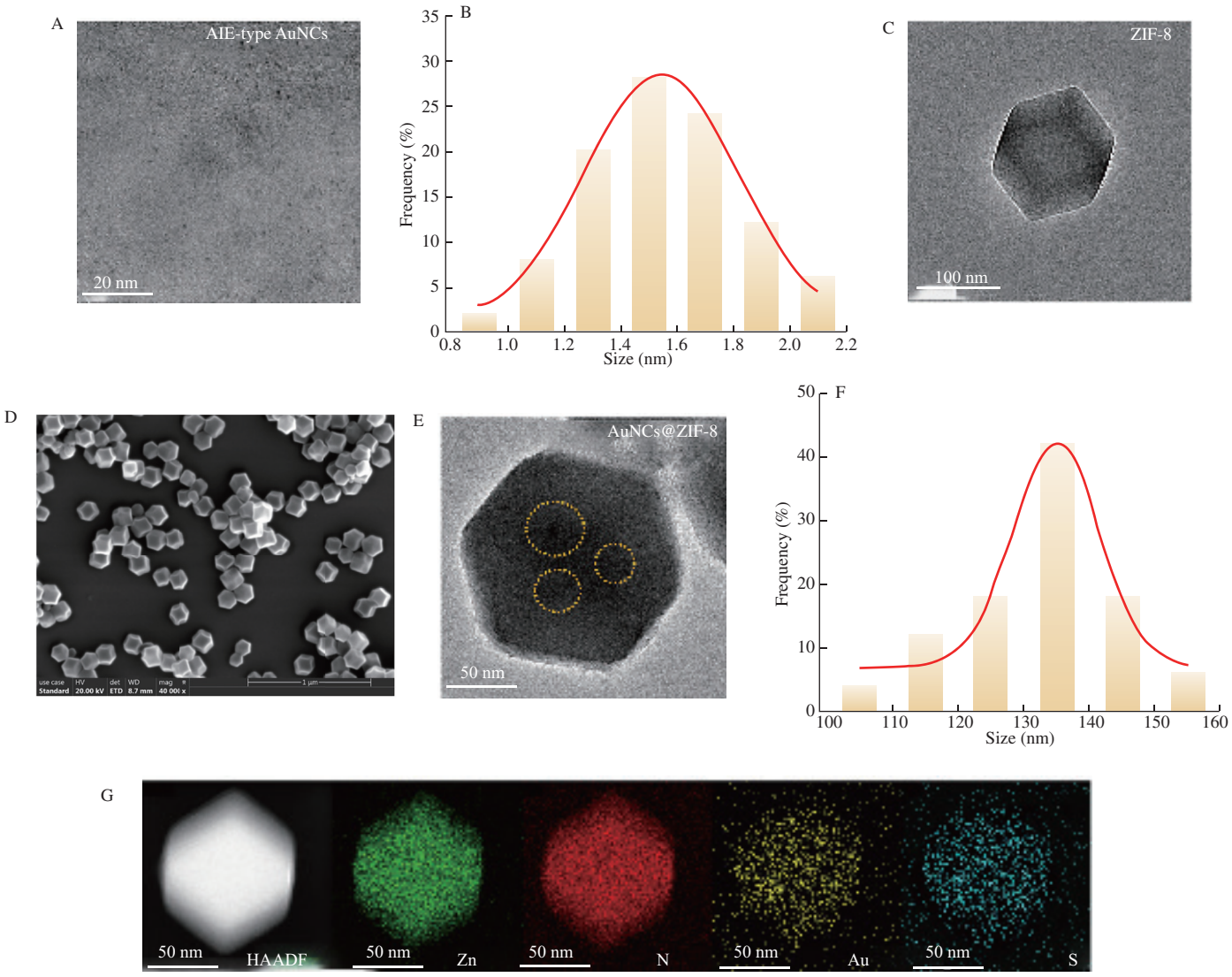

Fig. 2 TEM image (A) and size distribution diagram (B) of AuNCs; (C) TEM image of ZIF-8; SEM image (D), TEM image (E), particle size distribution (F), HAADF-STEM image and element mapping (N, Zn, Au, and S) (G) of AuNCs@ZIF-8.

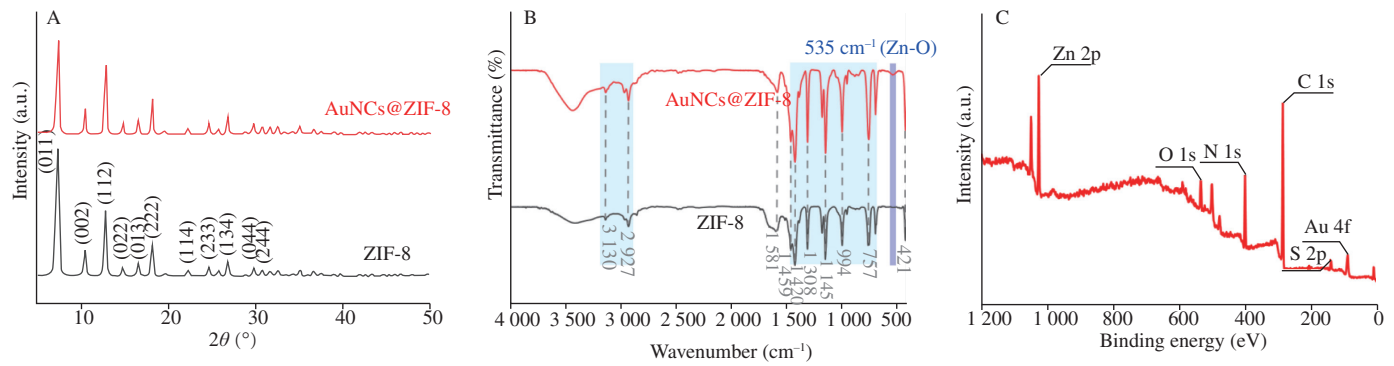

Fig. 3 (A) XRD spectra of AuNCs@ZIF-8 and ZIF-8; (B) FT-IR spectra of AuNCs@ZIF-8 and ZIF-8; (C) XPS spectrum of AuNCs@ZIF-8; XPS spectrum of (D) Au 4f and (E) Zn 2p for AuNCs@ZIF-8; (F) TGA spectra of AuNCs@ZIF-8 and ZIF-8.

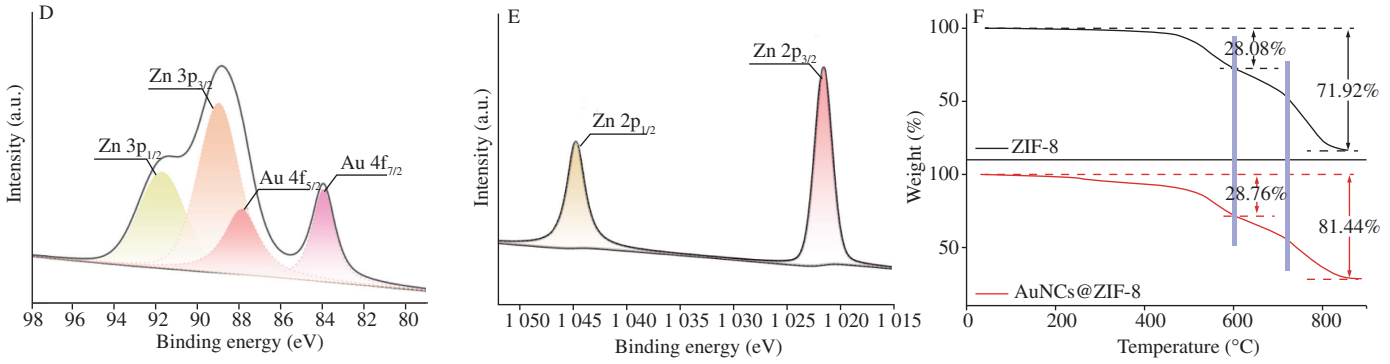

Fig. 3 (*Continued*)

from the AuNCs@ZIF-8 was derived from the encapsulated AuNCs, with the noted shift from 610 nm to 595 nm in E_M likely caused by the aggregation effects of AuNCs within ZIF-8 framework. The characteristic emission peaks of AuNCs in the supernatant at 400 nm almost disappeared after centrifugation of the AuNCs@ZIF-8 solution obtained from the reaction (Fig. S3), suggesting that the AuNCs were almost completely confined within the ZIF-8 framework. Furthermore, the fluorescence QY of the synthesized AuNCs and AuNCs@ZIF-8 materials were calculated to be 1.74% and 12.08%, respectively, using quinine sulfate (QS) as a reference (Fig. 4D).

The superior fluorescence properties of AuNCs were enhanced by the ZIF-8 framework, which also significantly improved their stability. Both the tolerance and storage stability of AuNCs@ZIF-8 under extreme conditions were investigated. Initially, both AuNCs@ZIF-8 and AuNCs underwent incubation at various temperatures (5−80 °C) for 1 h to assess their thermal resistance. As shown in Fig. 4E, following a 60 min heating period, the relative fluorescence intensity of AuNCs experienced a significant decrease as the temperature increased, contrasting with the relative fluorescence intensity of AuNCs@ZIF-8 remained essentially unchanged. Upon exposure to 365 nm UV irradiation for 60 min, the relative fluorescence intensity of AuNCs@ZIF-8 only decreased by 7.3% (Fig. 4F), further validating the superior stability conferred by ZIF-8 to AuNCs. Furthermore, Fig. 4G presented the fluorescence results of AuNCs and AuNCs@ZIF-8 solution after storage at 4 ℃ for 30 days. With the increase in storage time, there was a gradual decrease in the relative fluorescence intensity of AuNCs@ZIF-8, with it maintaining approximately 92.3% of its original value after 30 days. To assess the anti-photobleaching resistance, the relative fluorescence intensity of both was compared over 24 h, revealing a small enhancement in the anti-photostability of AuNCs with ZIF-8 encapsulation. This finding indicated that AuNCs@ZIF-8 exhibited higher reliability and longer lifespan under prolonged light exposure conditions. These results collectively demonstrated the remarkable stability of the AuNCs@ZIF-8 nanocomposite.

3.4 Conditions optimization for AuNCs@ZIF-8 synthesis

In order to optimizing the performance of the AuNCs@ZIF-8 nanocomposite, a detailed investigation into its preparation conditions was carried out. Organic solvents could induce the aggregation of the prepared AuNCs, thereby improving their encapsulation efficiency during forming the ZIF-8 framework. As shown in Fig. S4A, by varying the proportion of ethanol in the system (0−100%), it was found that the color of AuNCs solution was significantly different under visible light and ultraviolet irradiation, and determined that a 50% ethanol content yielded the strongest fluorescence intensity, which was the optimal conditions for maximizing the intramolecular vibration and rotation of the ligands on the surface of the AuNCs. Consequently, a 50% ethanol system, achieved by mixing equal volumes of ethanol with the AuNCs preparation solution, was utilized to eliminate unreacted reactants. The dosage of AuNCs served as a crucial factor affecting the fluorescence performance of AuNCs@ZIF-8. As illustrated in Fig. S4B, increasing the amount of AuNCs from 1.0 mL to 4.0 mL led to a significant enhancement in fluorescence. However, an excessive amount of AuNCs (5.0 mL) resulted in incomplete encapsulation within the ZIF-8 framework and diminished the fluorescence intensity. Maintaining the integrity and stability of the ZIF-8 structure was greatly dependent on the amount of Zn^{2+} ions and 2-MI. It was observed that the highest fluorescence intensity was achieved for the AuNCs@ZIF-8 nanocomposite prepared with the addition of 2-MI (10.0 mL, 90 mmol/L) when the dosage of Zn^{2+} ions was 10.0 mL, 30 mmol/L. Fig. S4C illustrated the variation in fluorescence intensity of AuNCs@ZIF-8 over reaction time. A progressive enhancement in fluorescence of AuNCs@ZIF-8 intensity was discernible within the 10−40 min (Fig. S4D). However, beyond a 40 min incubation period, the thickness of the ZIF-8 shell impeded both photon transmission and excitation of AuNCs, consequently eliciting a decline in fluorescence intensity. Consequently, the experimental conditions for the synthesis of the AuNCs@ZIF-8 nanocomposite were determined as follows: 4.0 mL of AuNCs, along with a combination of Zn^{2+} ions (10.0 mL, 30 mmol/L) and 2-MI (10.0 mL, 90 mmol/L) reactants, were employed, with an incubation time of 40 min.

3.5 Conditions optimization for detecting glucose using AuNCs@ZIF-8 probe

The impact of microenvironmental pH on AuNCs and AuNCs@ZIF-8 nanocomposite was investigated in PBS at varying pH values (3.0−11.0). The mixed systems were incubated at 37 °C for 60 min and analyzed the fluorescence responses. As shown in Fig. 5A, while the fluorescence of the AuNCs was largely unaffected by changes in the microenvironmental pH, there was a significant alteration in

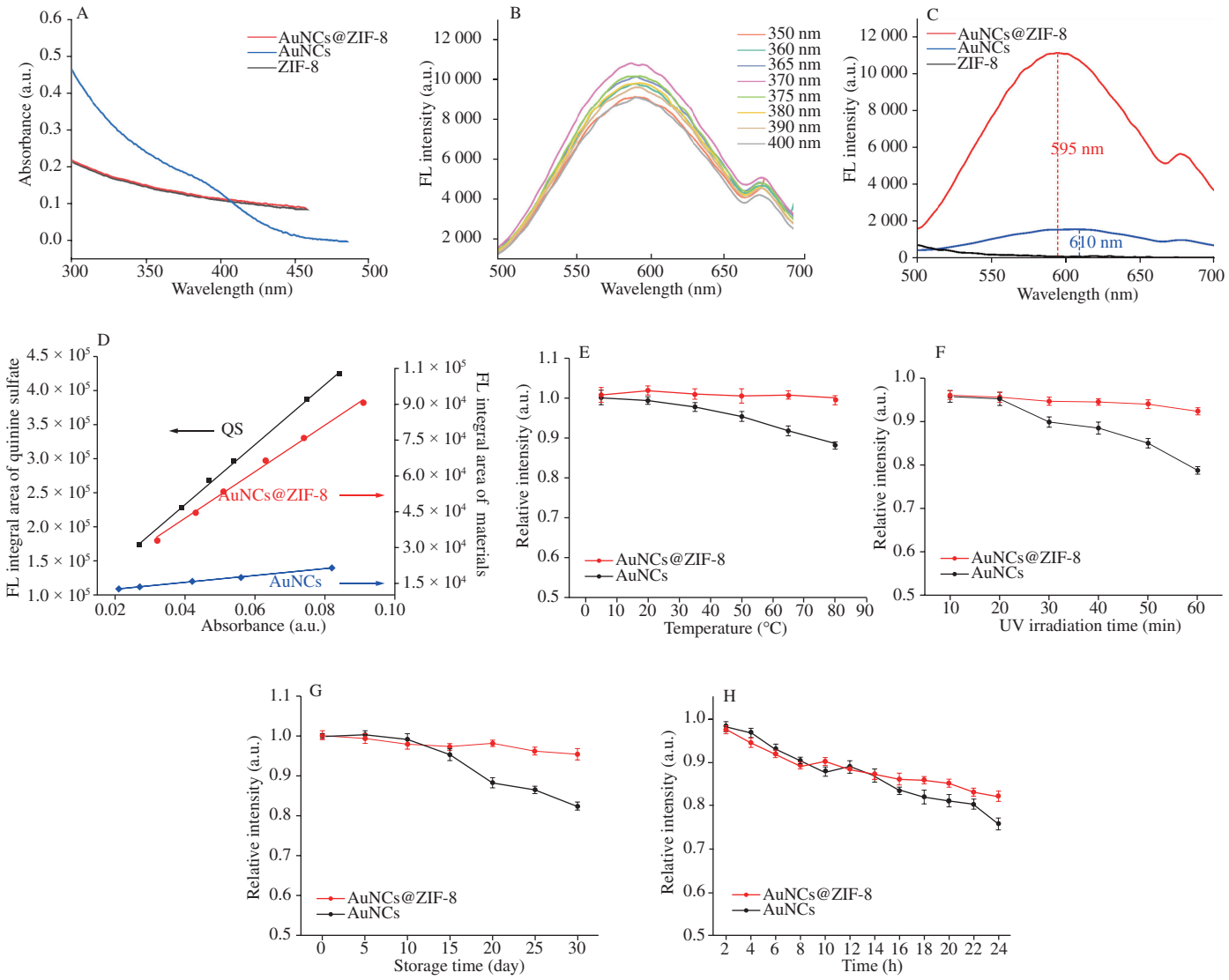

Fig. 4 (A) UV-visible spectrum of AuNCs@ZIF-8, AuNCs and ZIF-8; (B) Fluorescence spectra of AuNCs at different E_X; (C) Fluorescence emission spectra of AuNCs@ZIF-8, AuNCs and ZIF-8 (E_M: 370 nm); (D) The fluorescence QY of QS, AuNCs, AuNCs@ZIF-8; (E) Thermal stability of AuNCs@ZIF-8 and AuNCs at 5−80 °C; (F) Photostability of AuNCs@ZIF-8 and AuNCs under continuous irradiation at 365 nm for 10−60 min; (G) Fluorescence stability of AuNCs@ZIF-8 and AuNCs within 30 days; (H) Photobleaching resistance of AuNCs@ZIF-8 and AuNCs.

the fluorescence of the AuNCs@ZIF-8. Specifically, the Δ*F* of the AuNCs@ZIF-8 remained relatively stable in neutral and alkaline environments but exhibited a sharp decrease in acidic conditions, decreasing by 42.6% at pH 5.0 compared to pH 7.0. TEM analysis revealed that the rhombic dodecahedral structure of ZIF-8 was disrupted in the incubated system, with AuNCs being released around the disassembled ZIF-8 and resuming free movement (Fig. 5B). Therefore, the breakdown of ZIF-8 weakened its confinement effects on AuNCs under acidic conditions, causing the "turn-off" of their AIE effects and resulting in a reduction in Δ*F*. The pH sensitivity of AuNCs@ZIF-8 nanocomposite enabled the fluorescence behavior of AuNCs in the system to be synergistically regulated by pH and ZIF-8, providing a controllable mechanism for fluorescence detection.

As illustrated in Fig. 5C, separate mixtures of GOx and glucose with AuNCs@ZIF-8 were incubated at 37 °C for 60 min, resulting in nearly identical fluorescence spectra. However, upon their combination, a significant reduction in Δ*F* was observed in the AuNCs@ZIF-8 probe. This decrease was attributed to the catalytic action of GOx on glucose in the presence of oxygen, producing gluconic acid and H_2O_2, which reduced the system's pH. The reduction in Δ*F* occurred due to the sensitivity of AuNCs@ZIF-8 to acidity. To achieve high analytical performance for the glucose targets, various parameters were adjusted while maintaining a constant glucose concentration of 10 mmol/L, including the PBS of pH, incubation time and temperature and the amount of GOx added. As illustrated in Fig. S5A, the significant change in Δ*F* occurred at the PBS of pH at 6.5 which was chosen for experiments based on the stability and detection sensitivity of the AuNCs@ZIF-8. Upon adding a specific amount of GOx (4.5 U), the resulting Δ*F* gradually increased with increasing incubation time from 10 to 30 min and tended to stabilize after 30 min (Fig. S5B). Combined with the optimal results of temperature (37 °C) and GOx amount (2.7 U) presented in Figs. S5C and D, the conditions for detecting glucose targets using the AuNCs@ZIF-8 probe were ultimately determined.

3.6 Detection of glucose using AuNCs@ZIF-8 probe

The glucose detection capability of the synthesized AuNCs@ZIF-8 probe was evaluated under optimal experimental conditions. As depicted in Fig. S6, the fluorescence emission spectra were recorded from the reaction system for varying concentrations of glucose solutions (0−10 mmol/L). Upon E_X at 370 nm, the ΔF of the probe gradually decreased with the addition of glucose targets, accompanied by a slight red shift (E_M: 595−603 nm). The change in ΔF, denoted as F ($F_0 - F_i$), was determined by comparing the ΔF at a glucose concentration of 0 mmol/L (F_0) with that at a specific concentration (F_i).

As the glucose targets concentration increased, there was a corresponding gradual increase in the ΔF values, showing a strong linear relationship ($R^2 > 0.99$) within the glucose concentrations range of 0.5−10 mmol/L (Fig. 5D). The LOD determined at a signal-to-noise ratio of 3 (S/N = 3), was calculated to be 0.096 mmol/L. These findings demonstrated the precision, sensitivity, and usability of the designed AuNCs@ZIF-8 probe for detecting glucose targets. The relative standard deviation (RSD) of the fluorescence response ΔF for 5 batches of prepared AuNCs@ZIF-8 probe to the same concentration of glucose solution (5 mmol/L) was only 2.1% (n = 3), indicating excellent reproducibility and stability of the fluorescent probe throughout both preparation and application processes (Fig. 5E). The selectivity and interference resistance of the prepared AuNCs@ZIF-8 fluorescent probe for the glucose targets were further investigated. As shown in Fig. 5F, comparing the F values of the glucose targets at a concentration of 5 mmol/L, even with concentrations of fructose, galactose, sucrose, xylose, and maltose up to 15 mmol/L at the same conditions, F values were insignificant. This depended on the good and specific catalysis of glucose by the GOx. Meantime, various potential interfering substances, including urea, uric acid, ascorbic acid, and cysteine (5 mmol/L), were introduced into the reaction system. The findings revealed that the performance of the AuNCs@ZIF-8 probe remained excellent, regardless of the presence of the target glucose (5 mmol/L). Additionally, the influence of other reducing substances (serine and GSH, 5 mmol/L) and inorganic ions (Ca^{2+} and K^+, 5 mmol/L), was assessed, with results showing they had little impact on ΔF. Overall, the probe demonstrated outstanding specificity for glucose, providing accurate responses even in the presence of potential interferents.

3.7 Glucose analysis in real samples

The practical applicability of the prepared AuNCs@ZIF-8 fluorescent probe was evaluated by analyzing glucose levels in serums and glucose-containing beverages (Table 1). Fresh blood samples from 3 healthy volunteers were collected, centrifuged, and the resulting supernatant was analyzed for glucose content using the AuNCs@ZIF-8 probe. The results obtained an RSD of 2.0%−2.7% (n = 3), and showed a correlation coefficient of 0.99 with those obtained from a commercial glucometer (Fig. S7A). In the evaluation

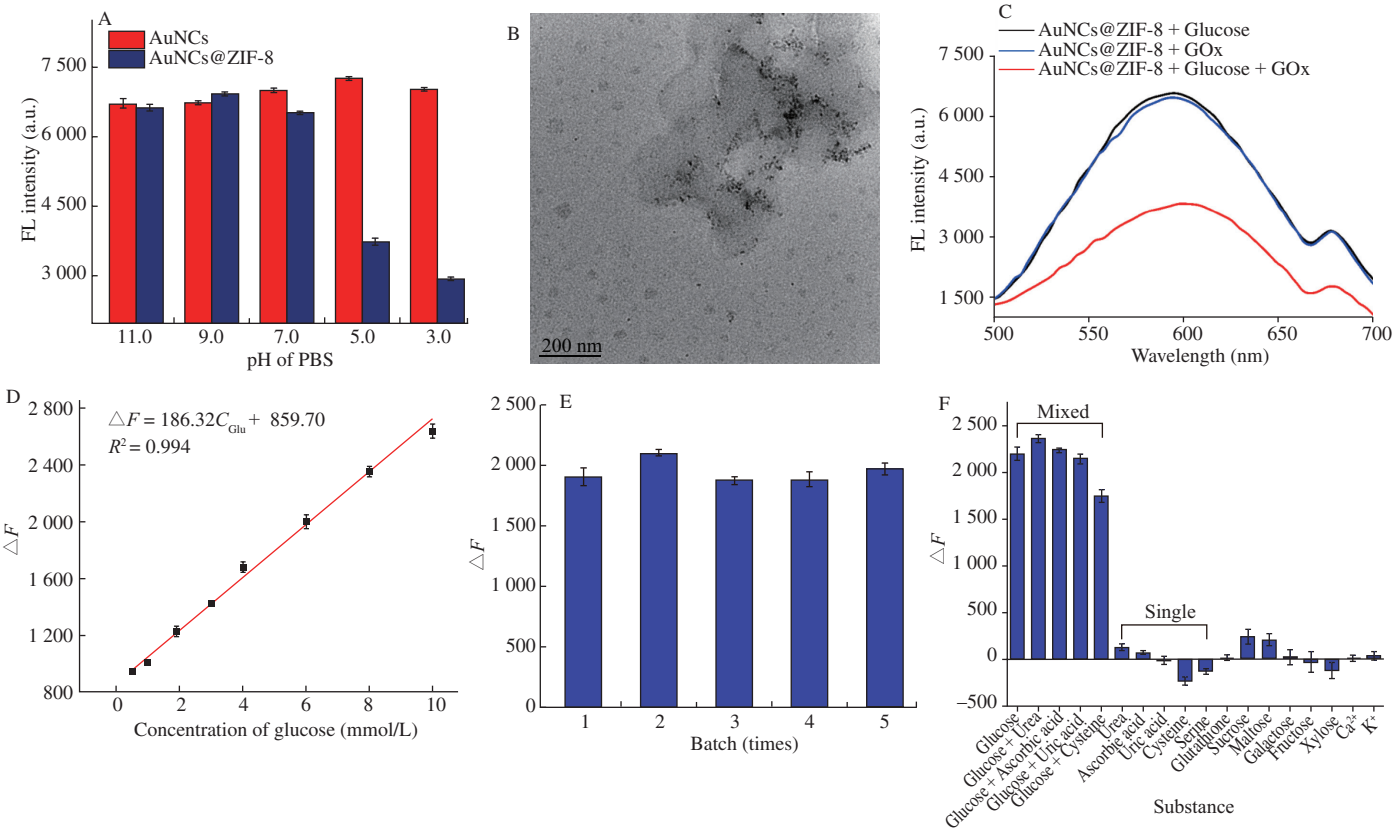

Fig. 5 (A) Fluorescence intensity of AuNCs@ZIF-8 and AuNCs incubated in PBS at different pH for 1 h; (B) TEM image of AuNCs@ZIF-8 after incubation in PBS at pH 5.0 for 30 min; (C) Fluorescence spectra of AuNCs@ZIF-8 + glucose, AuNCs@ZIF-8 + GOx, and AuNCs@ZIF-8 + glucose + GOx; (D) Calibration curve of the ΔF values of AuNCs@ZIF-8 versus glucose concentration; (E) Fluorescence response of AuNCs@ZIF-8 probe in 5 batches at concentrations of 5 mmol/L; (F) Fluorescence response to AuNCs@ZIF-8 probe of glucose (5 mmol/L), glucose structural analogues (15 mmol/L) and mixture of glucose and other substances (5 mmol/L).

of commercially available glucose beverages, the recoveries at 3 spiked concentrations (1.0, 4.0, and 7.0 mmol/L) fell within the range of 96.9%−104.3%, with an RSD of 1.8%−2.4% (n = 3), and demonstrated a correlation coefficient surpassing 0.99 compared to results obtained from a glucose content kit (Fig. S7B). These results demonstrated the feasibility of the proposed AuNCs@ZIF-8 probe for the detection of glucose targets in real samples. Compared to other strategies for glucose analysis based on different principles listed in Table 2, the proposed AuNCs@ZIF-8 probe demonstrated a broad linear range and a low LOD, providing reliable analytical results. Additionally, the detection process also offered significant cost advantages and did not require expensive and complex detection equipment. These advantages demonstrated the AuNCs@ZIF-8 probe presented an economical, sensitive, rapid, and convenient strategy for glucose quantification analysis.

Table 1
Detection results of glucose in serum and spiked beverages by AuNCs@ZIF-8 probe, glucometer method and glucose content kit method.

Samples		Initial concentration (mmol/L)	Spiked levels (mmol/L)	Total concentration (mmol/L)	AuNCs@ZIF-8 probe			Glucometer method or glucose content kit method	
					Found (mmol/L)	Recovery (%)	RSD (%, n = 3)	Found (mmol/L)	Recovery (%)
Serum	1	-	-	-	5.06	-	2.02	5.20	-
	2	-	-	-	6.31	-	2.67	6.40	-
	3	-	-	-	5.26	-	1.96	5.50	-
Beverage	1	1.46	1.0	2.46	2.54	107.86	2.04	2.39	93.46
			4.0	5.46	5.79	108.23	1.83	5.49	100.72
			7.0	8.46	8.70	103.42	3.22	8.55	101.30
	2	2.06	1.0	3.06	2.91	85.36	3.16	3.01	95.54
			4.0	6.06	5.87	95.36	2.48	6.18	103.42
			7.0	9.06	9.04	99.69	1.90	9.14	101.19
	3	2.46	1.0	3.46	3.38	92.24	3.19	3.52	106.09
			4.0	6.46	6.43	99.29	2.39	6.60	104.33
			7.0	9.46	9.53	101.05	2.32	9.63	102.36

Note: -, No spiked process in serum samples.

Table 2
Comparison of the proposed fluorescent probe with other reported glucose detection strategies.

Methods	Materials	LOD (mmol/L)	Liner range (mmol/L)	Sample	Reference
SERS	Au@Ag NPs	0.1	0.1−6	Urine	[30]
	Au NPs/Cu-TCPP(Fe)	0.004	0.16−8	Salivary	[9]
	4-MPBA/AgNP	0.1	1−10	Cell	[31]
	AgNP@cys/Au wafer@4-ATP	0.5	0.5−8	Serum	[32]
Electrochemical	ZnO: Co^{2+}	-	1−7	-	[33]
	Mn-NiO NSs/CC	0.000 6	0.002−2.14	Beverage	[34]
	PUC-PANI-ZnO@GOx	0.007	0.01−9.48	-	[35]
	ExGCP	0.812	2−8	-	[36]
	GOx/MnOxides/PE	0.29	0.56−5.55	Beverage	[37]
	MBE Grown VOx	0.32	1−10	-	[38]
Colorimetric	MnO_2	0.01	0.01−5	Serum	[39]
	Cu NSs-OPD-GOD	0.005 5	0.01−5	Beverage	[40]
	TiO_2/I_2/CMC (TIC)	0.4	0.5−10	-	[41]
Paper-based analytical	GOx	0.4	0.5−10	Glucose	[42]
	GOx-mediated sodium alginate gelation	1.4	1.4−7.0	Fruit	[43]
Fluorescence	BSPOTPE/BSA-AuNCs	0.1	1−8	Serum	[44]
	APBA-$CuInS_2$ QDs	0.001	0.005−8	Serum	[45]
	N-CDs@ZnO	0.25	1−6	Serum and blood	[46]
	BG-PAA/GOx	0.055	0.25−5	Beverage	[47]
	Au NCs@FGO	0.16	1−10	Serum	[48]
	AuNCs@ZIF-8	0.096	0.5−10	Serum and beverages	This work

Note: 4-MPBA, 4-Mercaptophenylboronic acid. Cu-TCPP(Fe), Cu-tetra (4-carboxyphenyl) porphyrin chloride (Fe (III)). CC, Carbon cloth. PUC, Polyurethane-chitosan. ExGCP, exfoliated graphite carbon paper. PE, pencil graphite electrode. MBE, molecular beam epitaxy. BSPOTPE, 1,2-bis[4-(3-sulfonatopropoxyl)phenyl]-1,2-diphenylethene. APBA, 3-aminophenylboronic acid. BG-PAA, brilliant-green sequestered poly (amic) acid. FGO, fluorescent graphene oxide.

4. Conclusions

In this study, a highly fluorescent AuNCs@ZIF-8 nanocomposite was successfully developed by capitalizing on the "AIE" effects of AuNCs and the domain-limiting effects provided by ZIF-8. Furthermore, the acidic environment resulting from GOx catalysis on glucose was utilized to induce the structural decomposition of ZIF-8, diminishing the confinement around AuNCs, preventing their aggregation, and facilitating accurate and rapid detection of glucose. The resulting pH-responsive fluorescent probe is not only simple to prepare and store but also highly accurate and rapid, providing an effective strategy for quantifying glucose levels in clinical samples and beverages. Future research may explore potential applications of this pH-responsive fluorescent probe across various fields.

Declarations of competing interests

Shuo Wang is an editorial board member for *Food Science and Human Wellness* and was not involved in the editorial review or the decision to publish this article. The authors declare no competing financial interest.

Acknowledgement

This work is supported by National Natural Science Foundation of China (32272416 and 31972147), Project of Tianjin Science and Technology Plan (22ZYJDSS00030) and Project Program of Key Laboratory of Tianjin Key Laboratory of Food Quality and Health, China (TJS202205). The authors are grateful to Research Centre of Modern Analytical Technology (TUST) for their help in instrument support.

Appendix A. Supplementary data

Supplementary data associated with this article can be found, in the online version, at http://doi.org/10.26599/FSHW.2024.9250392.

Reference

[1] X. Liu, D. Huang, C. Lai, et al., Peroxidase-like activity of smart nanomaterials and their advanced application in colorimetric glucose biosensors, Small. 15 (2019) 1900133. http://doi.org/10.1002/smll.201900133.

[2] H. Wang, W. Zhu, T. Xu, et al., An integrated nanoflower-like MoS_2@$CuCo_2O_4$ heterostructure for boosting electrochemical glucose sensing in beverage, Food Chem. 396 (2022) 133630. http://doi.org/10.1016/j.foodchem.2022.133630.

[3] V. Lind, N. Hammar, P. Lundman, et al., Impaired fasting glucose: a risk factor for atrial fibrillation and heart failure, Cardiovasc. Diabetol. 20 (2021) 227. http://doi.org/10.1186/s12933-021-01422-3.

[4] W. Ma, L. Xiao. H. Liu, et al., Hypoglycemic natural products with *in vivo* activities and their mechanisms: a review, Food Sci. Hum. Wellness 11 (2022) 1087-1100. http://doi.org/10.1016/j.fshw.2022.04.001.

[5] M. Mosslemi, N.D. Wong, Oral glucose tolerance test detects diabetes at early stages, Circulation 141 (2020) P441. http://doi.org/10.1161/circ.141.suppl_1.P441.

[6] Q. Lai, Q. Niu, C. Zhang, et al., Integrated Cu-Au stereo microelectrode arrays and microfluidic channels for the electrochemical detection of glucose, Food Chem. 432 (2023) 137229. http://doi.org/10.1016/j.foodchem.2023.137229.

[7] J. Yu, J. Wang, Y. Zhang, et al., Glucose-responsive insulin patch for the regulation of blood glucose in mice and minipigs, Nat. Biomed. Eng. 4 (2020) 499-506. http://doi.org/10.1038/s41551-019-0508-y.

[8] L. Yang, S. Wu, J. Wei, et al., A sensitive and simple HPLC-FLD-based method for the measurement of intracellular glucose uptake, Food Chem. 372 (2021) 131218 http://doi.org/10.1016/j.foodchem.2021.131218.

[9] S. Hu, Y. Jiang, Y. Wu, et al., Enzyme-free tandem reaction strategy for surface-enhanced raman scattering detection of glucose by using the composite of Au nanoparticles and porphyrin-based metal-organic framework, ACS Appl. Mater. Interfaces. 12 (2020) 55324-55330. http://doi.org/10.1021/acsami.0c12988.

[10] S. Chen, H. Huang, H. Sun, et al., Electrochemical sensor made with 3D micro-/mesoporous structures of CoNi-N/GaN for noninvasive detection of glucose, ACS Appl. Mater. Interfaces 14 (2022) 49035-49046. http://doi.org/10.1021/acsami.2c17325.

[11] P. Rai, S. Mehrotra, K. Gautam, et al., Polylactic acid/tapioca starch/banana peel-based material for colorimetric and electrochemical biosensing applications, Carbohydr. Polym. 302 (2022) 120368. http://doi.org/10.1016/j.carbpol.2022.120368.

[12] J. Ramos-Soriano, S.J. Benitez-Benitez, A.P. Davis, et al., A vibration-induced emision-based fluorescent chemosensor for the selective and visual recognition of glucose, Angew. Chem. Int. Ed. 60 (2021) 16880-16884. http://doi.org/10.1002/anie.202103545.

[13] S.F. Li, Y. Chen, Y.S. Wang, et al., Integration of enzyme immobilization and biomimetic catalysis in hierarchically porous metal-organic frameworks for multi-enzymatic cascade reactions, Sci. China Chem. 65 (2022) 1122-1128. http://doi.org/10.1007/s11426-022-1254-5.

[14] S. Qasemi, M. Ghaemy, Novel superabsorbent biosensor nanohydrogel based on gum tragacanth polysaccharide for optical detection of glucose, Int. J. Biol. Macromol. 151 (2020) 901-908. http://doi.org/10.1016/j.ijbiomac.2020.02.231.

[15] L. Sun, L.G. Chen, H.B. Wang, Fenton-like reaction triggered chemical redox-cycling signal amplification for ultrasensitive fluorometric detection of H_2O_2 and glucose, Analyst. 149 (2024) 546-552. https://doi.org/10.1039/D3AN01682J.

[16] L.G. Chen, L. Sun, N.N. Wu, et al., Cascade signal amplification strategy by coupling chemical redox-cycling and Fenton-like reaction: toward an ultrasensitive split-type fluorescent immunoassay, Analytica Chimica Acta. 1279 (2023) 341843. https://doi.org/10.1016/j.aca.2023.341843.

[17] H.B. Wang, A.L. Mao, T. Gan, et al., A turn-on fluorescence strategy for cellular glutathione determination based on the aggregation-induced emission enhancement of self-assembled copper nanoclusters, Analyst. 2145 (2020) 7009-7017. https://doi.org/10.1039/D0AN01247E.

[18] H.B. Wang, B.B. Tao, A.L. Mao, et al., Self-assembled copper nanoclusters structure-dependent fluorescent enhancement for sensitive determination of tetracyclines by the restriction intramolecular motion, Sens. Actuators B. 348 (2021) 130729. https://doi.org/10.1016/j.snb.2021.130729

[19] F. Liu, T.F. Yang, X.W. Chang, et al., Intelligent gold nanocluster for effective treatment of malignant tumor *via* tumor-specific photothermal-chemodynamic therapy with AIE guidance, Natl. Sci. Rev. 11 (2024). http://doi.org/10.1093/nsr/nwae113.

[20] F.Y. Mo, Z.Y. Ma, T.T. Wu, et al., Holey reduced graphene oxide inducing sensitivity enhanced detection nanoplatform for cadmium ions based on glutathione-gold nanocluster, Sens. Actuators B. 281 (2019) 486-492. https://doi.org/10.1016/j.snb.2018.10.133.

[21] Q.G. Shang, Y.Y. Liu, J. Ai, et al., Embedding au nanoclusters into the pores of carboxylated cof for the efficient photocatalytic production of hydrogen peroxide, J. Mater. Chem. A. 11 (2023) 21109-21122. http://doi.org/10.1039/d3ta03966h.

[22] J.D. Luo, Z.L. Xie, J.W.Y. Lam, et al., Aggregation-induced emission of 1-methyl-1,2,3,4,5-pentaphenylsilole, Chem. Commun. (2001) 1740-1741. http://doi.org/10.1039/B105159H.

[23] Z. Luo, X. Yuan, Y. Yu, et al., From aggregation-induced emission of Au(I)-thiolate complexes to ultrabright Au(0)@Au(I)-thiolate core-shell nanoclusters, J. Am. Chem. Soc. 134 (2012) 16662-16670. http://doi.org/10.1021/ja306199p.

[24] D.M. Qin, S. Meng, Y.S. Wu, et al., Aggregation-induced electrochemiluminescence resonance energy transfer with dual quenchers for the sensitive detection of prostate-specific antigen, Sens. Actuators B, 367 (2022) 132176. http://doi.org/10.1016/j.snb.2022.132176.

[25] J.L. Gao, X.D. Sun, Y.X. Liu, et al., Ultrathin metal-organic framework nanosheets (Cu-TCPP)-based isothermal nucleic acid amplification for food allergen detection, Food Sci. Hum. Wellness 12 (2023) 1788-1798. http://doi.org/10.1016/j.fshw.2023.02.031.

[26] X.Q. Zhang, Y. He, Z.T. Yuan, et al., A ph- and enzymatic-responsive nanopesticide to control pea aphids and reduce toxicity for earthworms, Sci. Total Environ. 861 (2022) 160610. http://doi.org/10.1016/j.scitotenv.2022.160610.

[27] S. Xie, Q. Liu, F. Zhu, et al., AIE-active metal-organic frameworks: facile preparation, tunable light emission, ultrasensitive sensing of copper (II) and visual fluorescence detection of glucose, J. Mater. Chem. C 8 (2020) 10408-10415. http://doi.org/10.1039/D0TC00106F.

[28] M. Guo, J. Chi, C. Zhang, et al., A simple and sensitive sensor for lactose based on cascade reactions in Au nanoclusters and enzymes co-encapsulated metal-organic frameworks, Food Chem. 339 (2020) 127863. http://doi.org/10.1016/j.foodchem.2020.127863.

[29] Y.H. Wang, Z.S. Shao, C. Cheng, et al., Fluorescent oligonucleotide indicators for ratiometric microrna sensing on metal-organic frameworks, Chem. Eng. J. 437 (2022) 135296. http://doi.org/10.1016/j.cej.2022.135296.

[30] Y. Lu, T. Zhou, R. You, et al., Fabrication and characterization of a highly-sensitive surface-enhanced raman scattering nanosensor for detecting glucose in urine, Nanomaterials. 8 (2018) 629. http://doi.org/10.3390/nano8080629.

[31] D. Koyel, G. Venkanagouda, K. Kiran, et al., Continuous *in-vitro* physiological glucose sensing for co-cultured 3D tumour spheroids using SERS based nano particle sensors (SERS-gNPS), Sens. Actuators B. 404 (2024) 135243. https://doi.org/10.1016/j.snb.2023.135243.

[32] C.C. Fu, S. Jin, J. Oh, et al., Facile detection of glucose in human serum employing silver-ion-guided surface-enhanced Raman spectroscopy signal amplification, Analyst. 142 (2017) 2887-2891. https://doi.org/10.1039/C7AN00604G.

[33] N. Ramachandra, A.N. Kumar, V.N. Yashwanth, et al., Green combustion synthesis of multifunctional inorganic ZnO: Co^{2+} (1−11 mol%) nanoparticles: electrochemical and photocatalytic applications, Inorg. Chim. Acta. 563 (2024) 121924. http://doi.org/10.1016/j.ica.2024.121924.

[34] L. He, J.Y. Su, T. You, et al., Mn incorporation boosted NiO nanosheets as highly efficient anode for sensitive glucose detection in beverage, LWT-Food Sci. Technol. 182 (2023) 114807. http://doi.org/10.1016/j.lwt.2023.114807.

[35] T. Chandni, J. Sagar Satish, K. Rohitash, et al., Fabrication of flexible glucose sensor based on heterostructure ZnO nanosheets decorated PU/Chitosan-PANI hybrid nanofiber, Microchem. J. 285 (2024) 109915. http://doi.org/10.1016/j.microc.2024.109915.

[36] T. Chandni, J. Sagar Satish, K. Rohitash, et al, Exfoliated graphite carbon paper-based flexible nonenzymatic glucose sensor, Mater. Sci. Eng.: B. 285 (2022) 115931. https://doi.org/10.1016/j.mseb.2022.115931.

[37] P. Paithoon, Y. Matinee, C. Kaweekarn, et al., Modified pencil graphite electrode as a low-cost glucose sensor, J. Sci-Adv. Mater. Dev. 5 (2020) 330-336. https://doi.org/10.1016/j.jsamd.2020.07.004.

[38] F. Filippo, P. Maria Recaman, K. Schouteden, et al., MBE grown vanadium oxide thin films for enhanced non-enzymatic glucose sensing, Advanced Functional Materials 33 (2023) 2304037. https://doi.org/10.1002/adfm.202304037.

[39] J. Zhang, X. Dai, Z.L. Song, et al., One-pot enzyme- and indicator-free colorimetric sensing of glucose based on MnO_2 nano-oxidizer, Sens. Actuators B. 304 (2019) 127304. http://doi.org/10.1016/j.snb.2019.127304.

[40] A.L. Han, Y.M. Zhao, J.H. Wu, et al., Self-assembled cop per nanoclusters used to mimic peroxidase for glucose detection, RSC Adv. 14 (2024) 3261-3266. http://doi.org/10.1039/d3ra07598b.

[41] B. Bansod Sneha, D. Ashutosh, R. Anju, Development of TiO_2-Based nanocomposite film for colorimetric detection of glucose, Mater. Sci. Eng.: B. 298 (2023) 116886. https://doi.org/10.1016/j.mseb.2023.116886.

[42] J. Aksorn, S. Teepoo, Development of the simultaneous colorimetric enzymatic detection of sucrose, fructose and glucose using a microfluidic paper-based analytical device, Talanta 207 (2019) 120302. http://doi.org/10.1016/j.talanta.2019.120302.

[43] H. Zang, X.Z. Li, Z.M. Qian, et al., Glucose oxidase-mediated sodium alginate gelation: equipment-Free detection of glucose in fruit samples, Enzyme Microb. Tech. 148 (2021) 109805. https://doi.org/10.1016/j.enzmictec.2021.109805.

[44] X. Wu, P. Wu, M. Gu, et al., Ratiometric fluorescent probe based on AuNCs induced AIE for quantification and visual sensing of glucose, Anal. Chim. Acta. (2020) 4. http://doi.org/10.1016/j.aca.2020.01.004.

[45] Z. Liu, L. Liu, M. Sun, et al., A novel and convenient near-infrared fluorescence “turn off-on” nanosensor for detection of glucose and fluoride anions, Biosens. Bioelectron. 65 (2014) 145-151. http://doi.org/10.1016/j.bios.2014.10.008.

[46] S. Yogita, P. Rajmani, K.S. Ajaya, et al., Highly fluorescent ZnO composite of N-doped carbon dots from *Dregea volubilis* for fluorometric determination of glucose in biological samples, J. Fluoresc. (2024) 3538. http://doi.org/10.1007/s10895-023-03538-z

[47] M. Maiga, I. Yazgan, V.M. Kariuki, et al., Brilliant green sequestered poly(amic) acid film for dual-mode detection: fluorescence and electrochemical enzymatic biosensor, Sens. Actuators B. 256 (2017) 71-78. http://doi.org/10.1016/j.snb.2017.10.002.

[48] S. Lei, Y. Liang, S. Qin, et al., A ratiometric fluorescent paper sensor for consecutive color change-based visual determination of blood glucose in serum, New J. Chem. 42 (2018) 6867-6872. https://doi.org/10.1039/C8NJ00502H.